Compact Irregular Conformal Phased Array: High-Gain Wide-Scan Onboard System for Enhancing UAV Communication

Yuanyan Su, Icaro V. Soares, Siegfred Balon, Jun Cao, Denys Nikolayev, Anja Skrivervik

▶ **To cite this version:**

Yuanyan Su, Icaro V. Soares, Siegfred Balon, Jun Cao, Denys Nikolayev, et al.. Compact Irregular Conformal Phased Array: High-Gain Wide-Scan Onboard System for Enhancing UAV Communication. IEEE Transactions on Vehicular Technology, 2024, pp.1-12. 10.1109/tvt.2024.3445456 . hal-04688799

HAL Id: hal-04688799
https://hal.science/hal-04688799v1

Submitted on 10 Oct 2024

HAL is a multi-disciplinary open access archive for the deposit and dissemination of scientific research documents, whether they are published or not. The documents may come from teaching and research institutions in France or abroad, or from public or private research centers.

L'archive ouverte pluridisciplinaire **HAL**, est destinée au dépôt et à la diffusion de documents scientifiques de niveau recherche, publiés ou non, émanant des établissements d'enseignement et de recherche français ou étrangers, des laboratoires publics ou privés.

Distributed under a Creative Commons Attribution - NonCommercial 4.0 International License

Compact Irregular Conformal Phased Array: High-Gain Wide-Scan Onboard System for Enhancing UAV Communication

Yuanyan Su, Icaro V. Soares, *Member, IEEE*, Siegfred Balon, Jun Cao, Denys Nikolayev, *Senior Member, IEEE*, and Anja K. Skrivervik

***Abstract*—This paper proposes a compact non-canonical non-uniform conformal phased array antenna (NNCPAA) attached to an irregular UAV surface to overcome the space and aerodynamic constraints for high-gain, wide-scan applications. The NNCPAA is parametrically determined using a geometric sequence for the *x*-axial spacings of array elements in the center rows to manipulate the elevation scan, while the *y*-axial spacings take care of the azimuth scan. It outperforms its equal-aperture uniform conformal counterpart before amplitude or phase synthesizing as it can achieve a lower sidelobe level, a smaller elevation-scan angle, and a wider 2D scanning coverage. Moreover, based on the proposed NNCPAA, a co-design method is developed for a compact high-performance onboard system at 5.8 GHz. By using improved miniature elements, the inter-element mutual coupling is reduced and all elements can be directly attached to the locally flat parts of the actual UAV surface, thus without any mechanical support added to the whole system. The experiments show that the onboard system achieves a peak gain of 21.8 dBi, a high efficiency of 88.4%, and scanning ranges exceeding 51° and ±28° with small scanning losses of 2.2 dB and 0.5 dB in elevation and azimuth, respectively. Therefore, the designed NNCPAA system is promising for UAV-based wireless communication (e.g., V2X) and remote sensing.**

***Index Terms* —Beamscanning, conformal array antenna, miniaturized antennas, non-uniform array, phased array, UAV communication.**

I. Introduction

VEHICLE-BASED communication and wireless sensing can provide more convenient and intelligent services for human beings, such as high-speed B5G communication, secure transportation, health care, life detection in natural disasters, environment monitoring, and military reconnaissance. For instance, automotive radar and millimeter-wave radar are typical in vehicle-to-vehicle (V2V) communication [1], [2]. As shown in Fig. 1, air-to-satellite (A2S) communication [3] enables the aircraft or fixed-wing unmanned aerial vehicle (UAV) as a relay to exchange information between satellites and user ends, to overcome the non-line-of-sight long transmission distance (more than 1000 meter) and enhance the system signal-to-noise ratio (SNR) [4]. These vehicles benefit from a sufficient power supply and stable and reliable communication over a long time duration. They are also promising in microwave imaging and sensing for glacier movement, climate change, and scientific research. Small UAVs are used more often in vehicle-to-unmanned aircraft (V2UA) at 5.02~5.09 GHz, vehicle-to-everything (V2X) at 5.905~5.925 GHz, and dedicated short-range (DSR) communications from 5.85 GHz to 5.925 GHz [5], [6], [7], [8], [9]. In these scenarios, rotary-wing drones are advantageous in the simple, low-cost, high-flexibility, on-demand deployment. However, they suffer from small payload and short battery life for short-range communication. Furthermore, most radiating systems are planar structures, for which the windage and aerodynamics are not considered in the design [10]-[18]. In this regard, these systems are vulnerable to the harsh weather and environment, whilst an extra bulky radome can be employed for protection purposes.

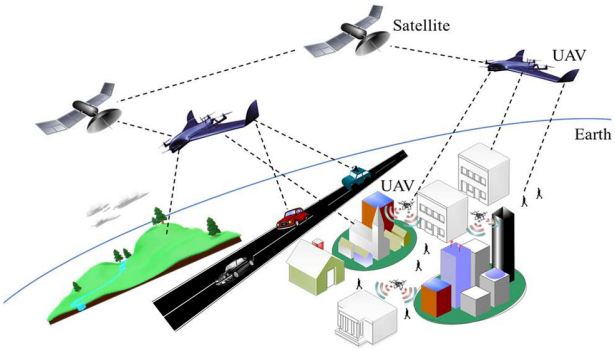

Fig. 1. Application scenarios of UAV-based communication and radar sensing.

Manuscript is submitted on August 15, 2024 for final submission. This work was supported by Armasuisse Projects (No. 8003518609, 8003521510, 8003525429, 8003529739, and 8003532452) in Switzerland. (*Corresponding author: Yuanyan Su*)

Y. Su is with the College of Integrated Circuits, Nanjing University of Aeronautics and Astronautics, and was with the Microwave and Antenna Group, Ecole Polytechnique Fédérale de Lausanne, 1015 Lausanne, Switzerland (e-mail: su_yuanyan@nuaa.edu.cn).

I. V. Soares and D. Nikolayev are with the CNRS, IETR—UMR 6164, University of Rennes, 35000 Rennes, France (e-mail: icaro.soares@ieee.org; denys.nikolayev@cnrs.fr).

S. Balon is with the Innovation and Technology Center, Desay SV Automotive Singapore Pte. Ltd., 609935 Singapore, Singapore (e-mail: siegfred.balon@desaysv.com).

J. Cao is with Neuroscience Research Australia, The University of New South Wales, 2031 Randwick, Australia (e-mail: j.cao@neura.edu.au).

A. K. Skrivervik is with the Microwave and Antenna Group, Ecole Polytechnique Fédérale de Lausanne, 1015 Lausanne, Switzerland (e-mail: anja.skrivervik@epfl.ch).

Copyright © 20xx IEEE. Personal use of this material is permitted. However, permission to use this material for any other purposes must be obtained from the IEEE by sending a request to pubs-permissions@ieee.org.

Accepted manuscript

Therefore, we focus on the fixed-wing UAV or glider, as illustrated in Fig. 1 and Fig. 2. The following challenges will be addressed for these UAV communication and sensing systems.

- An accurate element position $\boldsymbol{r}_i$ and aligned normal vector $\hat{\boldsymbol{n}}_i$ on the UAV surface for aerodynamic purposes;
- A small starting angle in elevation scan, i.e., $|\theta_{\text{scan}}|$ should be as small as possible to enlarge the footprint on the earth ground;
- A low sidelobe level (SLL);
- A wide two-dimensional (2D) scanning coverage with limited element number;
- A high gain with a small array aperture confined in an area of 130×80 mm^2 in *xoy*-plane, i.e., a high aperture efficiency.

The applications mentioned above rely on advanced antenna technologies. Specifically, multibeam or beamscanning antennas are highly demanded to achieve flexible directive beams towards the user terminals and sensing targets. One approach to realizing such beam control is through ray optics, using lens antennas with mechanical feeds or spacial feeds with minimal RF electronics. Examples include conventional dielectric plano-convex lens antennas, recent metalens antennas, transmit-array antennas, and metasurface antennas [19]. Another convenient method for beamscanning involves utilizing a phased array antenna (PAA) with a beamforming network (BFN). This method offers advantages in a fast, continuous, and arbitrary beam control, while its antenna architecture and design procedure are much simpler. Leveraging mature RF electronic technologies, PAA emerges as a promising candidate, especially in the low and medium microwave bands.

On the other hand, to tackle the additional space and aerodynamic constraints imposed by the UAV, conformal array antennas (CAAs) have been developed in the literature. In contrast to the planar arrays, CAAs can be easily accommodated on a non-flat platform such as the wing, nose, base, and tail of the aircraft, with no need for extra space, and meet the aerodynamic requirements. Most proposed CAA systems feature convex shapes, for instance, cylindrical arrays [20]-[33], spherical arrays [33]-[37], hemispherical arrays [38]-[40], wing-shaped arrays [41]-[43], and pyramidal arrays [44]. These convex conformal arrays are able to reduce the blind zone of the planar array effectively. They also can widen the scanning range when the array element has directive radiation, because a convex surface allows for more elements to take over the directivity at the scanning edge.

Until now, the majority of the existing CAA designs have concentrated on the theoretical analysis, topological synthesis, and optimization algorithm, rather than encompassing the entire PAA system design. This omission neglects considerations for the physical antenna layer, frame/platform scattering effects, and system deployment. Some work with the experimental validation includes a spherical CAA to achieve the orbital angular momentum (OAM) vortex beams with a bulky BFN [34], a concave hemispherical-like CAA that requires

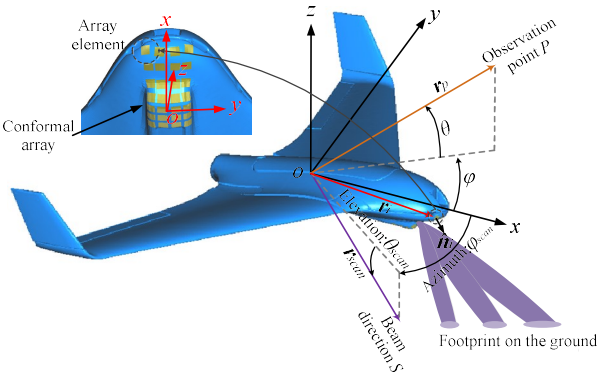

Fig. 2. Illustration of the proposed NNCPAA conformed to a non-canonical UAV surface.

multilayer structures and complicated mechanical support [45], and self-adapting conformal antennas to compensate the phase difference for spherical surfaces [35]. Some cylindrical CAAs have been also designed to acquire the omnidirectional radiation patterns [29], [32], the enhanced axial radiation [21], and the end-fire radiation [24], but lacking the high gain and the beamscanning ability. In contrast, a low-profile wide-scan sectoral CAA can achieve a high gain and a ±60° scanning range in a single principal E-plane [22]. A slotted substrate-integrated-waveguide (SIW) array based on a modified Rotman lens has been investigated to obtain a ±46° scanning range in E-plane, associated with a relatively low aperture efficiency [23]. A millimeter-wave microstrip CAA attached to a cylinder has been developed with a limited beam-scanning ability, by using a simplified beam-switching feeding network [25].

However, most of these prior arts require a large element spacing of at least half-wavelength and thus are not suitable for a miniature CAA. An electrically small conformal antenna proposed in [26] looks interesting for CAA miniaturization, but it generates an end-fire pattern and does not support a continuous beam scanning. Also, the array design and the system design are treated as separate entities, lacking a cohesive co-design method for the entire CAA system. Furthermore, irregular surfaces may be necessary due to the structural design of the UAV itself. For example, the antennas need to be installed beneath the front head of the aircraft, as shown in Fig. 2. This sophisticated surface features both convex and concave parts, creating a more complex environment for the array elements to radiate effectively. The array factor is no longer valid in the conformal array synthesis, and the field cancellation due to different surface curvatures may lead to reconfiguring the array topology. To the best of the authors' knowledge, there is a limited discussion about designing, analyzing, and implementing a UAV-shaped phased array that addresses the comprehensive system requirements.

In this paper, a novel array topology based on geometric sequence is introduced to design a compact non-canonical non-uniform conformal phased array antenna (NNCPAA) for high-gain and wide-scan applications. The parametric geometry of the NNCPAA is designed and optimized under the aerodynamic and space constraints to reduce the SLL, lower the starting elevation-scan angle θ_{scan}, and widen the 2D scanning coverage. Moreover, a light compact high-gain onboard system is co-

Accepted manuscript

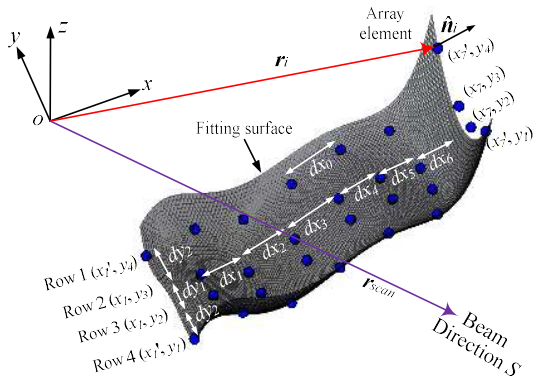

Fig. 3. Geometry definition and modeling of the theoretical NNCPAA on the fitting non-canonical UAV surface.

designed in conjunction with the proposed NNCPAA. The miniaturization of the single-layer elements with low cross polarization (X-pol) levels allows for direct attachment to the locally flat UAV surface without extra mechanical support, thus simplifying the architecture of the onboard system.

This paper is structured as follows. The theoretical NNCPAA is proposed in Section II, where a parametric study is performed to identify its key parameters and the far-field performance is discussed with a comparison to its uniform counterpart. The implementation of the proposed NNCPAA and the co-design of the whole onboard system are described in Section III, which also elucidates the design details of the array element and the BFN board. Section IV presents the fabrication and measurement of the integrated onboard system, with concluding remarks in Section V.

II. Design Principle of NNCPAA

While the position and orientation of the array elements on the UAV surface can be decided using some existing algorithms individually, the sheer number of parameters for optimization can hinder the convergence of results. For this reason, an alternative, efficient, and computationally cost-effective NNCPAA parametrically determined by a geometric sequence is first proposed. Compared to the uniform array, this array topology introduces more design degrees of freedom to address the problems specified in Section I.

It is also noted that the inter-element mutual coupling and the embedded element pattern are usually considered in the uniform array synthesis. However, in the case of NNCPAA, plenty of pre-knowledge regarding the separation-varying mutual coupling and the embedded element patterns based on different element locations and orientations is redundant. In this paper, we will demonstrate that the simple isolated element pattern and the rapidly streamlined design method can yield acceptable accuracy in estimating the implemented array performance in the full-wave simulation, while avoiding the analysis of mutual coupling and embedded element patterns in a complicated environment.

A. Geometry Design of NNCPAA

To guarantee the array elements fixed on the actual UAV surface with the aligned normal vectors at their positions, a polynomial fitting to the UAV surface is employed to define the position $\boldsymbol{r}_i$ and normal vector $\hat{\boldsymbol{n}}_i = (\theta_i, \varphi_i)$ of each element analytically. The fitting uses 235 sampling points to include both concave and convex features of the surface. As shown in Fig. 3, the polynomial fitting function in Cartesian coordinates is expressed as

$$\begin{aligned} z = f(x,y) = {} & p_{00} + p_{10}x + p_{01}y + p_{20}x^2 + p_{11}xy + p_{02}y^2 \\ & + p_{30}x^3 + p_{21}x^2y + p_{12}xy^2 + p_{03}y^3 + p_{40}x^4 \\ & + p_{31}x^3y + p_{22}x^2y^2 + p_{13}xy^3 + p_{04}y^4 \\ & + p_{50}x^5 + p_{41}x^4y + p_{32}x^3y^2 + p_{23}x^2y^3 \\ & + p_{14}xy^4 + p_{05}y^5 \end{aligned} \quad (1)$$

in which the polynomial coefficients summarized in Table I are generated by using a curve fitting toolbox in MATLAB. The order of the polynomial in (1) is chosen in such a way as to ensure the fitting root mean square error (RMSE) lower than 0.002. The coordinate origin in Fig. 3 is the center of the whole UAV structure, which is the same as in Fig. 2. The blue dots indicate the elements characterized by the normal vector $\hat{\boldsymbol{n}}_i$ and the element position $\boldsymbol{r}_i$ that relates to the element number and the element spacings dx_n (n = 0, ..., N-1, where N = 7) and dy_m (m = 1, 2).

TABLE I
Polynomial Coefficients of the Fitting Function for the Non-Canonical UAV Surface

Coeff.	Value	Coeff.	Value	Coeff.	Value
p_{00}	−1.56	p_{11}	-7.6×10^{-4}	p_{23}	2.56×10^{-3}
p_{01}	2.91×10^{-5}	p_{12}	−176.33	p_{30}	3816.20
p_{02}	−2.83	p_{13}	8.08×10^{-4}	p_{31}	-3.04×10^{-2}
p_{03}	-1.38×10^{-4}	p_{14}	−32267.84	p_{32}	−14489.35
p_{04}	2704.54	p_{20}	−619.89	p_{40}	−11480.56
p_{05}	3.42×10^{-3}	p_{21}	7.27×10^{-3}	p_{41}	0.047
p_{10}	48.89	p_{22}	4228.10	p_{50}	13628.35

Given that the conformal area is confined to 130×80 mm^2 in xoy-plane and the four corner elements must be positioned at the boundary of the conformal area, the maximum row number of the array along y axis cannot exceed 4, when the element spacing larger than the element size is considered.

In this NNCPAA, the x coordinates of the first elements in the two center/inner rows are defined as x_1, and the x-axial element spacing follows a geometric sequence written as:

$$dx_n = dx_1 \cdot q^{n-1}, (n = 2, \dots, N-1) \quad (2)$$

in which the initial term dx_1 is the first element spacing, q is the common ratio, and N is the total element number in the x direction. Then the x coordinates of the rest of the elements in the two inner rows can be derived using:

$$x_{n+1} = x_n + dx_n, (n = 1, \dots, N-1). \quad (3)$$

In the meantime, it is found that the two outer-row elements with a constant spacing dx_0 perform better than other geometry distributions. Hence, dx_0 is defined as equal to the x-axial distance between the two corner elements (x_N'-x_1') divided by N-1, i.e.,

$$dx_0 = \frac{x_N' - x_1'}{N-1}. \quad (4)$$

To determine the y coordinates of the array elements, the y-axial spacings are denoted as the variables dy_1 and dy_2, since the conformal surface is symmetric with respect to the xoz-plane. Then, dy_2 becomes (y_4-y_1-dy_1)/2 to keep the elements located at

Accepted manuscript

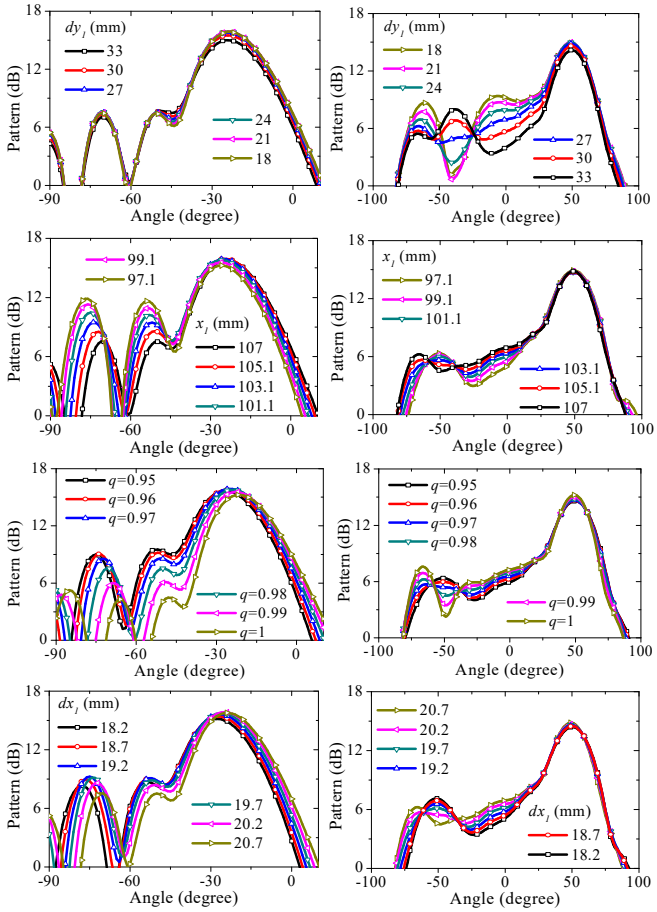

(a) Elevation plane (b) Azimuth plane

Fig. 4. Parametric study of the proposed theoretical NNCPAA for the irregular UAV surface. When one parameter is tuned, the rest parameters are fixed.

the boundary of the conformal area. In this way, a fully parametric geometry is established for the NNCPAA, and there is a total of four parameters (dx_1, q, x_1, and dy_1) to be studied.

To expedite the calculation of the far-field pattern for this NNCPAA, an in-house code developed from [46] and [47] is utilized, with the calculation of one scanning angle in less than 2 seconds and the consideration of element polarization pattern and coordinate transformation for polarization conversion. However, the detailed algebraic derivation of the code is omitted in this paper for brevity. Furthermore, to enlarge the scanning range of a compact array, the $\cos^2$ pattern is proved as a good candidate with the broad beamwidth, thus employed here for the y-polarized array element.

B. Parametric study

To identify the key parameters for the elevation and azimuth scanning radiation, a parametric study on the proposed NNCPAA operating at 5.8 GHz (ISM band) is conducted. As depicted in Fig. 4, the y-direction spacing dy_m is dominant to the sidelobe and grating lobe performance in azimuth. Meanwhile, the x-direction related parameters, especially q, can slightly adjust the sidelobe tail further away from the main lobe (so that this tail moves outside the main lobe scanning region) in that plane. The optimal dy_1 to achieve the minimum SLL is 27 mm.

TABLE II
OPTIMIZED PARAMETERS OF THE PROPOSED THEORETICAL NNCPAA

Parameter	Value	Parameter	Value
dx_1	20.7 mm	dy_1	27 mm
x_1	107 mm for Rows 2 & 3 96.1 mm for Rows 1 & 4	dy_2	24.1 mm
q	0.98	$N_{y\times x}$	4×7

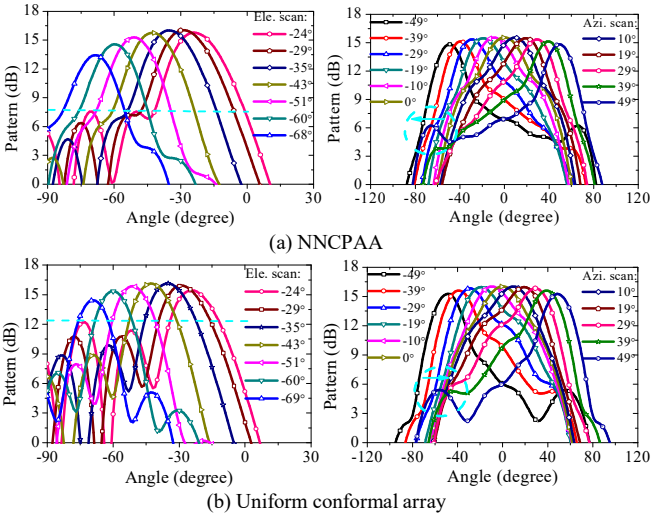

(a) NNCPAA

(b) Uniform conformal array

Fig. 5. Pattern comparison of different CAAs at 5.8 GHz using same phase definition corresponding to elevation ($\varphi_{scan} = 0°$) and azimuth ($\theta_{scan} = -47°$) scan.

In contrast, the elevation scanning performance is seldom perturbed by dy_1. It is solely determined by the x-direction related parameters. In particular, the increase in x_1 can significantly suppress the high sidelobes, decrease the elevation-scan angle, and enhance the antenna gain at the low elevation angles simultaneously. Besides, by tuning q and dx_1, the element number along x direction and the best position for the two inner-row elements can be found, such that the elements close to the surface edge can take a good scanning control for the low elevation angle. Therefore, an optimal array topology can be determined through several parametric sweeps. Note that the radiation pattern for x_1 = 97.1 mm reveals a substantially high SLL in the elevation scan and a closer distance between the sidelobe and the main lobe for the azimuth pattern, as its topology is similar to the uniform array.

The optimized parameters of this theoretical NNCPAA are tabulated in Table II, with the aim of lowering the starting elevation-scan angle and widening the 2D scanning coverage that stipulates the SLL of < -8 dB in elevation. After that, both the position and normal vector of each element can be obtained based on these four parameters. It is interesting to find that the normal vector of the edge element is inclined within 30° with respect to the center one to maintain the curvature stability and the horizontal polarization for azimuth scan is dominant, such that the vertical polarization takes less effect on the array's far-field performance. In this way, the polarization purity in azimuth scan can be guaranteed for the NNCPAA.

C. Performance Discussion

To demonstrate the advantages of the proposed NNCPAA, a uniform conformal array with the equal spacing of dx = 20.8

Accepted manuscript

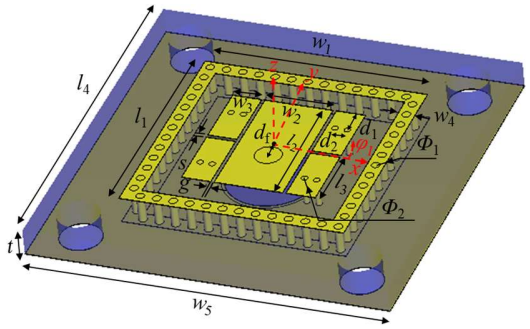

Fig. 6. Configuration of the improved miniature microstrip array element.

TABLE III
PARAMETERS OF THE OPTIMIZED MINIATURE ARRAY ELEMENT

Par.	Value (mm)	Par.	Value (mm)	Par.	Value (mm)	Par.	Value (mm)
w_1	10.8	w_5	17.5	l_1	10.8	Φ_1	0.4
w_2	3.3	d_1	1.26	l_2	6.44	Φ_2	0.3
w_3	1.38	d_2	0.59	l_3	3.12	g	0.19
w_4	0.8	d_f	0.7	l_4	17.5	s	0.19

mm and dy = 25 mm to ensure the same fitting surface is compared. Fig. 5 plots the scanning patterns of these two conformal arrays in two cutting planes. As can be seen, the NNCPAA can achieve an azimuth scan range of $-49° \le \varphi_{scan} \le 49°$ and an elevation scan range of $-68° \le \theta_{scan} \le -24°$ with a small scanning loss of < 0.75 dB and < 2.6 dB, respectively. The maximum gain of 16 dBi occurs at the scanning angle of (φ_{scan} = 0°, θ_{scan} = -29°) and is comparable to the uniform array. However, unlike the uniform array, its SLL of -8.24 dB in the elevation scan is 5 dB lower than that of the uniform array. On the other hand, the highest azimuth sidelobes of the NNCPAA at two scanning edges are manipulated almost outside the main-beam scanning region of ±49°, thus minimizing their impact on main lobe performance. The NNCPAA also effectively reduces the large sidelobe tails present in the uniform array. Besides, it is worth noting that even compared to a uniform planar array under the conditions of the same array aperture, same element number, and without synthesis methods either on element phase or magnitude, the proposed NNCPAA still takes the advantages of a lower SLL, a smaller starting elevation-scan angle, a wider scanning range, and better aerodynamic performance.

III. NNCPAA REALIZATION AND CO-DESIGN OF ONBOARD SYSTEM

A. Array Element Design

To realize the broad-beam $\cos^2$ pattern and minimize the element spacing for a compact array, a miniaturized single-layer microstrip antenna initially proposed in [48] is further improved so that it can be used as an attachable array element. As illustrated in Fig. 6, besides the patch size, the slots and the metallic pins enable an increase in the antenna design's degree of freedom and a significant reduction in the resonant frequency of the original square patch. The outer copper strips and the periodic posts are used to suppress the surface wave and the resultant mutual coupling to its neighbors, while the radiation performance of the central microstrips remains unchanged. The substrate is TMM10i with a thickness of t = 1.27 mm (0.025λ_0),

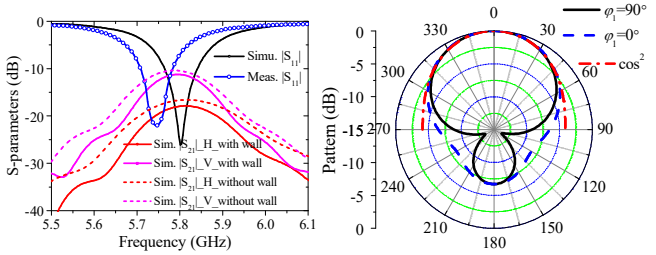

(a) S-parameters (b) Radiation patterns

Fig. 7. Input impedance matching, mutual coupling, and radiation patterns (at 5.8 GHz) of the improved miniature microstrip array element.

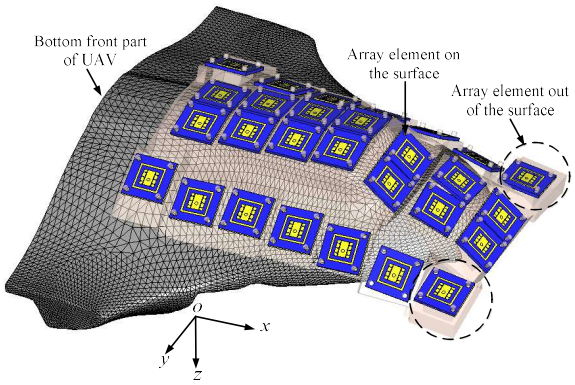

Fig. 8. Configuration of the implemented NNCPAA on the partial UAV.

a dielectric constant of 9.8, and a tangential loss of 0.002 at 10 GHz. The optimized parameters are given in Table III, and the overall microstrip size excluding the outer isolator is merely 6.44×6.44 mm^2 (0.12×0.12λ_0^2) at 5.8 GHz.

Fig. 7 plots the simulated far-field patterns of this array element at 5.8 GHz and compares its S-parameters with those of the original antenna without the outer isolator. Two elements are separated with a small distance of 18 mm (~0.35λ_0) to assess the coupling performance. As can be seen, in both the horizontal and vertical arrangements, the mutual coupling within the input impedance bandwidth of 77 MHz is 1 to 2 dB lower than that of the original antennas. The boresight gain reaches 4.11 dBi at 5.8 GHz with a 1dB gain flatness bandwidth from 5.75 GHz to 5.86 GHz and a low front-to-back ratio of 6.73. The broad beamwidths of 112.6° and 104.6° in the planes of φ_1 = 0° and φ_1 = 90° are achieved and contribute to a wide beamscanning for the whole array. The X-pol level of this element especially within the main-lobe region is less than –42.3 dB and –68 dB in the planes of φ_1 = 0° and φ_1 = 90° accordingly. Hence, these low X-pol levels can help suppress the X-pol patterns of the whole array at the array element level. Overall, the pattern shape of the proposed element in the upper plane aligns with the $\cos^2$ pattern as desired in Section II.

B. NNCPAA Design

Based on the positions and normal vectors of the 28 elements specified from Section II, the NNCPAA can be easily constructed in *CST Studio Suite*, a commercial full-wave simulation, as shown in Fig. 8. However, to guarantee the elements of the two inner rows placed on the protruding UAV bottom, dy_1 is further reduced to 18 mm, the theoretical SLL in the azimuth scan is thus slightly increased to –9.6 dB as a trade-off. Nevertheless, the scanning performance of the final

Accepted manuscript

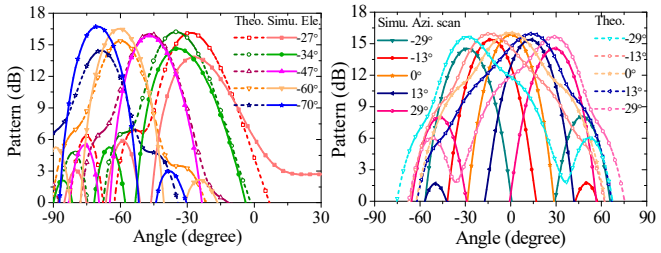

(a) Elevation scan (b) Azimuth scan

Fig. 9. The theoretical and simulated (in implementation) beamscanning performance of the proposed NNCPAA in elevation and azimuth.

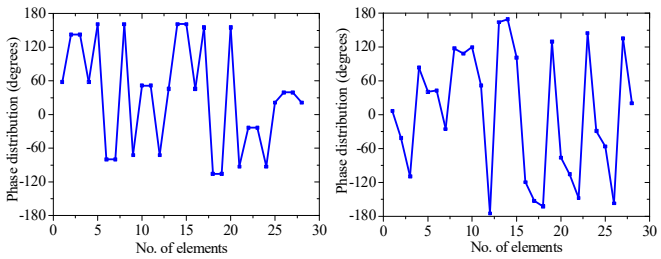

(a) $\varphi_{scan} = 0°$, $\theta_{scan} = -30°$ (b) $\varphi_{scan} = -50°$, $\theta_{scan} = -45°$

Fig. 10. Element phase distribution of the implemented NNCPAA for the steering angle of ($\varphi_{scan} = 0°$, $\theta_{scan} = -30°$) and ($\varphi_{scan} = -50°$, $\theta_{scan} = -45°$).

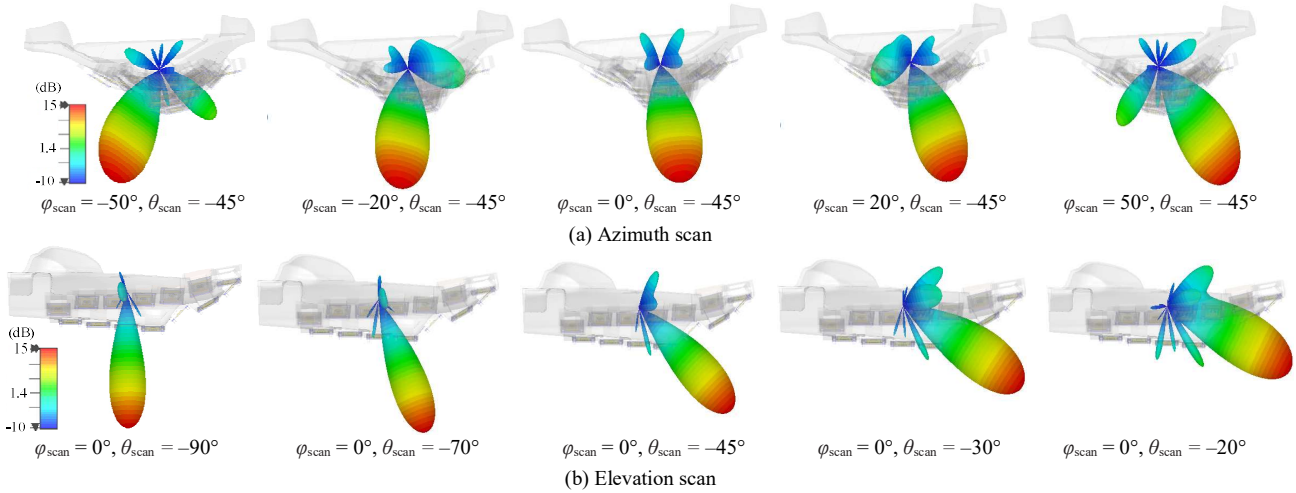

Fig. 11. 3D scanning patterns of the implemented NNCPAA on the non-canonical UAV surface in azimuth and elevation.

NNCPAA still preserves in both two main principal planes, i.e., $\varphi_{scan} = 0°$ and $\theta_{scan} = -45°$, as compared in Fig. 9. Due to the fitting error of the UAV surface, the two front corner elements are physically located outside the UAV surface, but they are still included here for the completeness of concept validation. The simulation has proven that these two elements can be removed with little influence on the NNCPAA's scanning performance in two principal planes.

As shown in Fig. 9, a 2D beam scanning range of $-89° \leq \theta_{scan} \leq -27°$ (62°) in elevation and $-29° \leq \varphi_{scan} \leq 29°$ in azimuth is achieved with a scanning loss of 3 dB and 1.4 dB, respectively. A wider azimuth scanning range (e.g., ±37°) is attainable but with a little higher scanning loss and SLL. While the mutual coupling ignored in the theoretical patterns will marginally increase the scanning loss and SLL (~3 dB) of the implemented NNCPAA, the scanning pattern shapes of the implemented NNCPAA align reasonably well with the theoretical ones. Notably, the azimuth sidelobes induced by the mutual coupling remain outside the main-lobe scanning region and have little impact on the azimuth scanning performance. Therefore, the validation suggests that mutual coupling can be reasonably neglected during the theoretical design in Section II.

The element phase distribution required for a scanning angle (φ_{scan}, θ_{scan}) can be calculated using the expression of $e^{jk\boldsymbol{r}_i \cdot \boldsymbol{r}_{scan}}$, where $\boldsymbol{r}_{scan}$ is the coordinates of the specified scanning beam direction. For example, the phase distribution for the scanning angles ($\varphi_{scan} = 0°$, $\theta_{scan} = -30°$) and ($\varphi_{scan} = -50°$, $\theta_{scan} = -45°$) is depicted in Fig. 10. The three-dimensional (3D) scanning patterns of the implemented NNCPAA are presented in Fig. 11 for the elevation and azimuth scans. The maximum gain of 15 dBi occurs at $\theta_{scan} = -80°$ in the elevation, associated with an aperture efficiency of 76%.

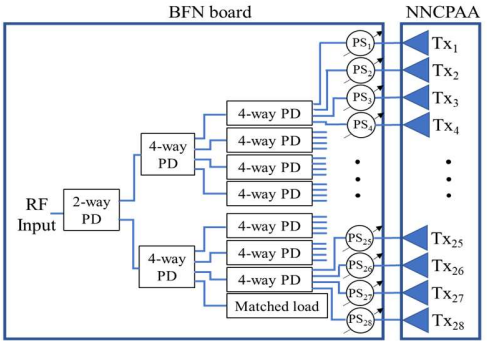

Fig. 12. Schematic diagram of the designed onboard system.

C. Co-Design of Onboard System

System deployment should be considered when the antenna system is designed for UAV-based applications, as the UAV framework and the BFN architecture made by large printed-circuit-board (PCB) panel(s) will have significant influences on the radiation and scanning performance of the isolated antenna array due to the superposition of the reflected waves. To this end, a co-design method for the onboard system is investigated with the designed NNCPAA. The entire architecture of the proposed onboard system is illustrated in Fig. 12 and Fig. 13(a).

Accepted manuscript

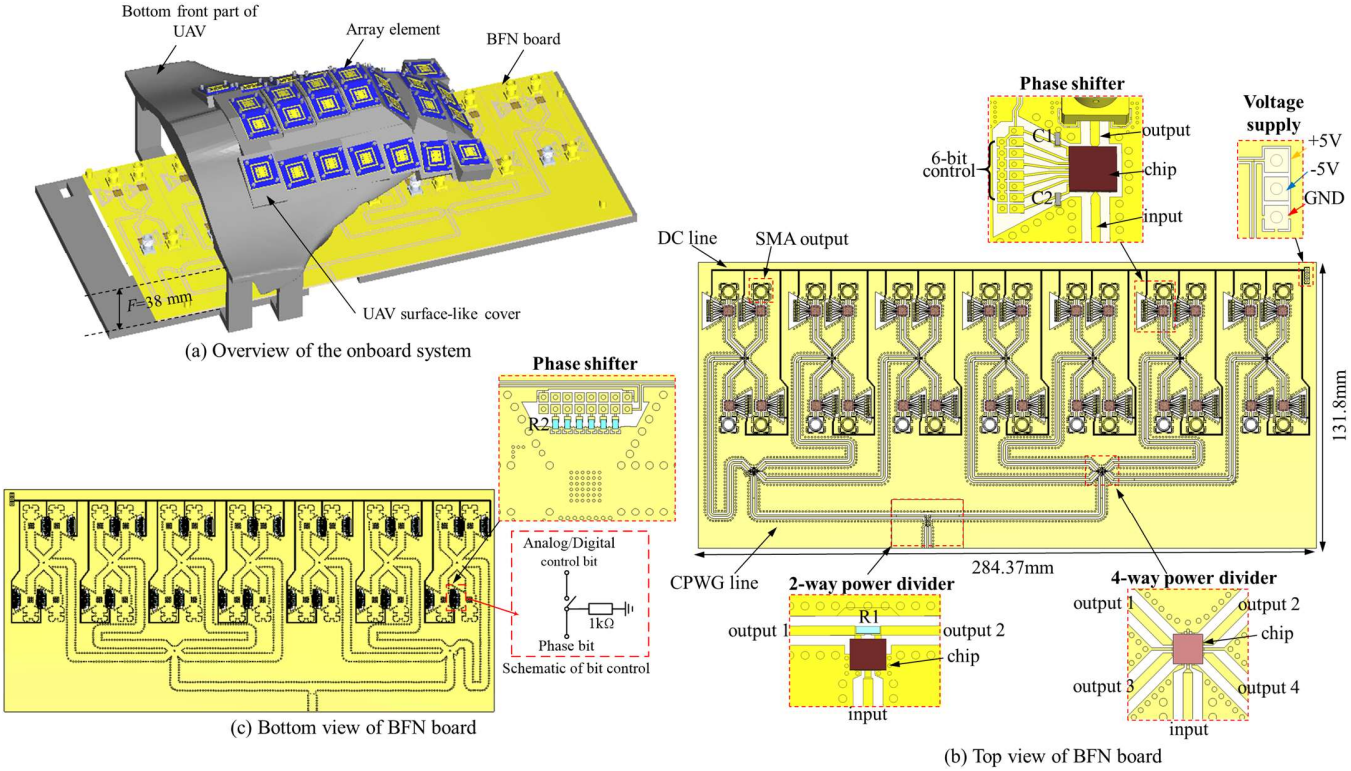

Fig. 13. Configuration of the whole onboard system with the partial UAV body.

It mainly comprises the upper NNCPAA and a single BFN board below to realize the required amplitude and phase for each element. Noted that the ultra-thin UAV surface-like cover is only used for testing and debugging purposes here, it can be removed because it is designed to have the almost same normal vectors of the actual UAV surface.

We found that the BFN board can also serve as a ground plane to further improve the antenna efficiency, since its size is roughly twice larger than the NNCPAA. To achieve the goal, the distance F between the NNCPAA and the BFN board must be optimized to maximize the antenna gain. According to our study, the maximum gain of the embedded array element can be improved to 8 dBi when F is optimized to 38 mm. Hence, the maximum gain for the total 28 elements can reach as high as 22.5 dBi in theory.

The designed BFN board consists of 28 digital phase shifters [49] and 10 power dividers, nine of which are 4-way power dividers [50] and one of which is a 2-way Wilkinson power divider [51]. Considering the space limitation on the BFN board and a continuous 360°phase control for each element, all these functional devices are designed using the integrated circuits (ICs), as shown in Figs. 13(b-c). Since the digital phase shifters are active, a ±5V DC power supply is required, and a versatile design to realize the phase bit control is sketched in Fig. 13(c) for both external analog and digital bit control uses.

To simplify the system architecture, the layouts of DC signals and RF signals are designed on a single PCB board. The mutual coupling between the RF transmission lines and the DC lines is suppressed by using the grounded co-planar waveguide (CPWG) transmission lines. Moreover, to consider the bending effect from the curved transmission-line segments, the physical lengths of the RF transmission lines are optimized to ensure the minimum phase difference at the inputs of the 28 phase shifters. In this design, the optimized physical length for each branch is equivalent to each other, and the corresponding line width is 0.96 mm printed on the TMM10i substrate.

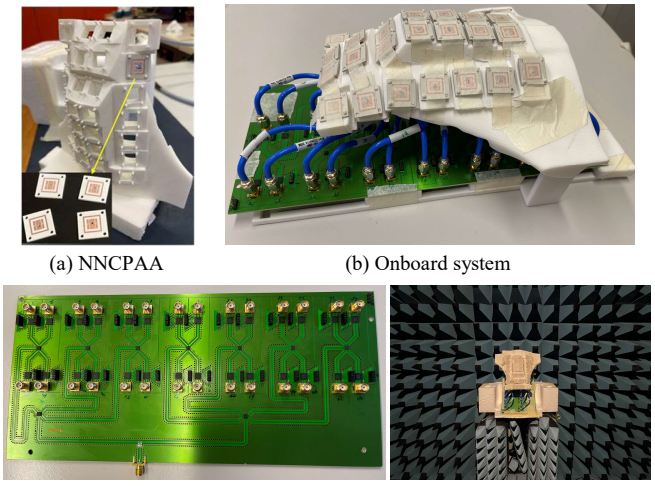

Fig. 14. Fabrication prototypes of the proposed NNCPAA, BFN board, and the entire onboard system and pattern measurement setup in anechoic chamber.

IV. Fabrication and Experimental Validation

A. Fabrication Prototypes

Fig. 14 presents the fabrication prototypes of the proposed NNCPAA and the entire onboard system manufactured in collaboration with Atelier de fabrication de Circuits Imprimés

Accepted manuscript

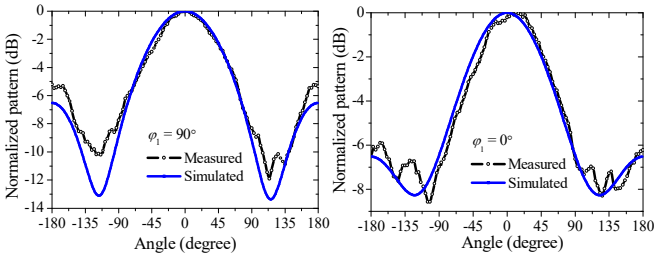

(a) Patterns in φ_1=90° (b) Patterns in φ_1=0°

Fig. 15. Measured and simulated radiation patterns of the array element at the operating frequency of 5.72 GHz.

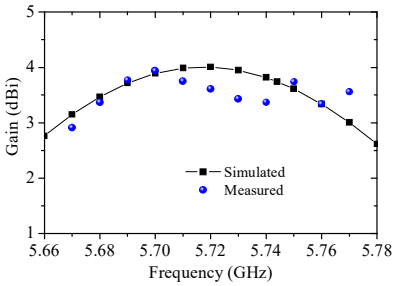

Fig. 16. Measured and simulated antenna gain of the proposed array element over frequency.

(ACI) workshop and Atelier de Fabrication Additive (AFA) workshop at École Polytechnique Fédérale de Lausanne. The dielectric cover and the UAV model are 3D printed using SLS (laser powder fusion) technology for the experimental tests. Alternatively, these light and small array elements can be easily soldered or glued on the UAV surface without mechanical support in the final assembling system. The far-field pattern measurement is performed in an anechoic chamber as shown in Fig. 14(d).

The S-parameter measurement of the fabricated BFN board reveals that apart from the insertion losses of the power dividers and phase shifters, an additional loss of ~1.5 dB is introduced from the mismatch of the feeding lines on the circuit board and the bent semi-rigid cables connecting to the array elements.

B. Performance of Antenna Element

The measured input impedance matching of the fabricated array element is plotted in Fig. 7(a) and compared with the simulated one. The measured resonant frequency is slightly shifted down, because of the fabrication tolerances on the slots and the patch size. These parameters are also sensitive to the radiation performance due to the narrow 80 MHz impedance bandwidth. Therefore, the radiation pattern measurement and the subsequent onboard antenna system measurement are conducted for the actual operating frequency of 5.72 GHz. Besides, the resonance of the array element before and after it was attached to the UAV surface is almost identical. Thus, the UAV surface effect is negligible to the antenna resonance.

The measured radiation patterns of the array element in two orthogonal principal planes are exhibited in Fig. 15, which shows good agreement with the simulated results. Both the measurement and the simulation have verified that the proposed array element can successfully achieve a wide beamwidth of >109° and >101° in the plane of φ_1 = 0° and φ_1 = 90°,

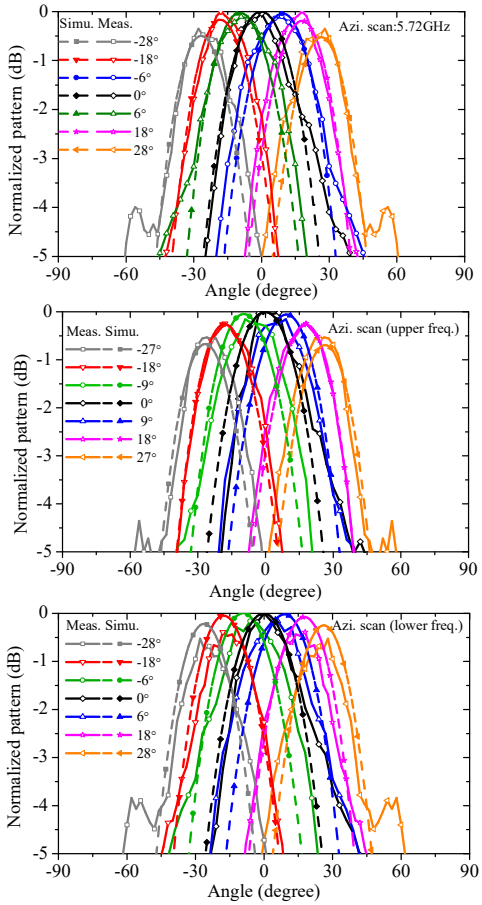

Fig. 17. Measured and simulated scanning patterns of the designed onboard antenna system at different frequencies in the azimuth scan when θ_{scan} = –45°.

respectively. The measured 1dB gain flatness bandwidth is more than 100 MHz with a peak gain of 3.94 dBi, as shown in Fig. 16. It is noted that some ripple will appear in the radiation pattern of an embedded array element due to the essential characteristic of the electrically small element and the large UAV surface effect. However, its main beam shape is still reasonably matched to that of the isolated array element or the $\cos^2$ pattern. Therefore, using a constant $\cos^2$ pattern for the theoretical NNCPAA design is reasonable and more convenient, as evidenced in Fig. 9. Also, a constant pattern can help avoid the huge pre-knowledge of different embedded element patterns for an irregular conformal surface from the time-consuming full-wave simulation.

C. Performance of Onboard Antenna System

Since the full-wave simulation of the actual onboard antenna system is extremely difficult especially when a lot of bent semirigid cables in a limited space are considered, we experimentally validate the far-field performance of this onboard antenna system and compare it with the simulated patterns of the NNCPAA with a mimic ground plane and the theoretical maximum gain as estimated in Section III-C. To ensure precise phase distribution for the conformal phased array inputs, it is imperative to compensate for the phase differences arising from several factors. These factors include the bent

Accepted manuscript

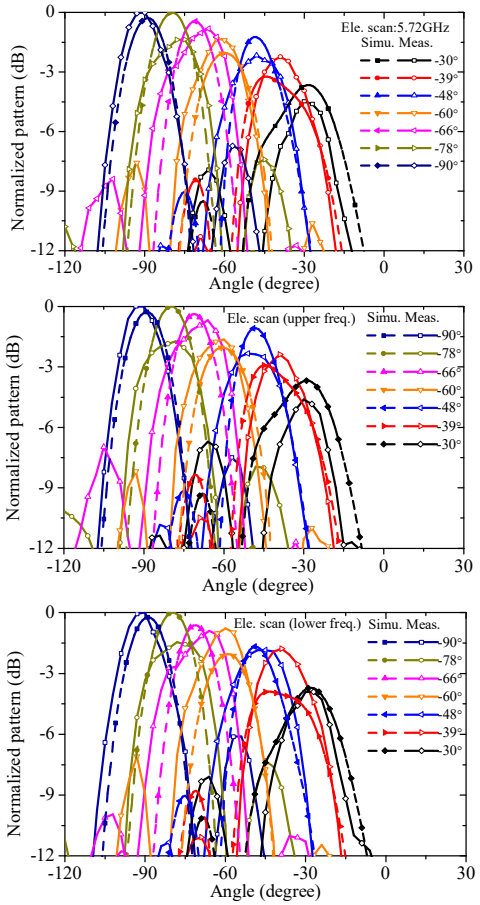

Fig. 18. Measured and simulated scanning patterns of the designed onboard antenna system at different frequencies in the elevation scan when $\varphi_{scan} = 0°$.

semirigid cables, fabrication tolerances on the BFN board, phase variations from the ICs, and the effects of the soldering mask. Calibration of the outputs from the bent semirigid coaxial cables connecting to the 28 phase shifters is thus essential before their use. This calibration process helps mitigate the discrepancies and guarantee accurate phase alignment across the conformal phased array.

Figs. 17-18 compare the measured and simulated far-field scanning patterns of the onboard antenna system in the azimuth and elevation planes at different working frequencies. It is shown that at the frequency of 5.72 GHz, the designed onboard NNCPAA system can eventually achieve a scanning range of $-90° \le \theta_{scan} \le -39°$ for elevation and $-28° \le \varphi_{scan} \le 28°$ for azimuth within a very small scanning loss of 2.2 dB and 0.5 dB, respectively. The measured elevation pattern at $\theta_{scan} = -30°$ looks more different from the simulated one, especially in terms of its high SLL, reduced gain, and narrowed beamwidth. This is probably caused by the misalignment between the AUT (antenna under test) and the reference horn antenna. The measured maximum antenna gain is 21.8 dBi at $\theta_{scan} = -90°$, which is 6.8 dB higher than the simulated gain of the NNCPAA alone in Fig. 9 and approaches the theoretical maximum gain reported in Section III-C. Therefore, it is experimentally verified that the designed BFN board at its best distance can serve as an additional reflector to improve the antenna gain,

TABLE IV
X-POL LEVELS OF THE PROPOSED ONBOARD SYSTEM FOR DIFFERENT SCANNING ANGLES

Scanning angle	Elevation scan		Azimuth scan		Highest X-pol level
	$\theta_{scan}=-30°$ $\varphi_{scan}=0°$	$\theta_{scan}=-90°$ $\varphi_{scan}=0°$	$\theta_{scan}=-45°$ $\varphi_{scan}=0°$	$\theta_{scan}=-45°$ $\varphi_{scan}=30°$	
Simulated X-pol level	–41.8 dB	–47 dB	–46.6 dB	–25 dB	–18.7 dB
Measured X-pol level*	–32.6 dB	–43 dB	–21.1 dB	–24 dB	–14 dB

*Noted that the discrepancy between the measurement and the simulation is mainly caused by the scattering effects from the close semirigid cables that are not considered in the simulation.

yielding a high antenna efficiency of 88.4% for the whole onboard antenna system.

The presence of the BFN board and the shaped semirigid cables close to the NNCPAA would lead to a little higher sidelobes and pattern distortion. Also, the slight discrepancy between the simulated and the measured beam directions may result from the phase discretization errors from the phase shifter ICs. More importantly, different from the matching loads used for the simulated array elements, the imperfect input impedance matching of the measured array elements may cause the multi-reflections of the input signals and induce the second radiation, hence altering the specified magnitude and phase for the array elements in theory and deteriorating the simulated pattern shape.

To assess the X-pol performance, the simulated and measured X-pol levels of the center and scanning-edge patterns in two principal planes are compared in Table IV. According to the table, the measured X-pol level of the whole onboard system within the concerned 1dB-beamwidth region is lower than –14 dB both for the elevation and azimuth scan. It is thus reasonably good for a very compact CAA and the polarization purity in elevation scan is much better than that in azimuth scan. Other possible solutions to further decrease the azimuthal X-pol level and the gain loss from the polarization mismatching in future could be:

- some algorithms for the phase control or both the magnitude and phase controls (if the system complexity is not the main requirement) to synthesize the X-pol level, such as particle swarm optimization, alternating projection-based methods, genetic algorithms, differential evolution method, least-squares method, and convex optimization;
- using the switching method with reconfigurable elements (e.g., adding PIN diodes) to turn on the regional elements having positive contributions, while digitally switching off the rest based on the polarization requirement along a certain direction;
- optimizing the element rotation;
- replacing the current miniature single-polarized elements with new investigated dual-polarized/circular-polarized elements. Also, the polarization diversity can be utilized, combining with the current design method.

Nevertheless, the measurement results match reasonably well with the simulated ones. The SLLs in the elevation scans

Accepted manuscript

TABLE V
PERFORMANCE COMPARISON OF DIFFERENT CONFORMAL ARRAY SYSTEMS

	[45]	[35]	[34]	[22]	[23]	This work
Volume	$3.6\times3.6\times1.32\lambda_0^3$	$2.2\times1.6\lambda_0^2$	$7.3\times7.7\times7\lambda_0^3$	$5.6\times1.1\times0.55\lambda_0^3$	$3.1\times4.2\times0.84\lambda_0^3$	$2.7\times1.8\times0.78\lambda_0^3$
Element spacing	$>0.81\lambda_0$	$0.45\lambda_0$	$\sim0.77\lambda_0$	$0.48\lambda_h$	$0.51\lambda_0$	$0.35\lambda_0$
Max. gain	16.1 dBic	N.A.	N.A.	17.52 dBi	19.3 dBi	21.8 dBi
Antenna efficiency	~31.8%	N.A.	N.A.	N.A.	~33.1%	88.4%
Conformal type	Concave hemi-sphere	Sphere	Sphere	Cylinder	Cylinder	Irregular
BFN	yes	yes	yes	no	no	yes
2D scanning ability	yes	yes	yes	possible	no	yes
Scanning range (ele./azi.)	±90°/ ±90°	N.A.	±90°/ ±90°	±60°	±46°	>51°/ >±28°
Highest SLL	-5.6dB	-8dB	N.A.	-8dB	-9dB	-6.1dB

are comparable to the simulations. Meanwhile, the azimuth sidelobes are still beyond the targeted main-beam scanning region and have negligible effects on the main lobe performance in that plane. Furthermore, Table V compares the main performance and features of the proposed onboard NNCPAA system with those of the state-of-the-art conformal array systems. The comparison indicates that the proposed NNCPAA, along with its onboard system, is a good candidate as a compact, high-gain, high-efficiency solution for UAV-based wide-scan applications, especially when the conformal surface is irregular. In conclusion, the experimental validation underscores the advantages and cost-effectiveness of the proposed NNCPAA topology and co-design method.

V. CONCLUSION

In this work, we introduce a novel compact non-uniform phased array antenna conformed to a non-canonical UAV surface. Operating in the ISM band around 5.8 GHz, this antenna aims to achieve high gain and wide 2D beamscanning coverage while minimizing sidelobe levels. The non-uniform array topology, determined parametrically using a geometric sequence, increases design flexibility without resorting to time-consuming optimization algorithms. Additionally, the paper explores a co-design method for a compact high-gain onboard system in conjunction with the proposed NNCPAA. The implemented onboard NNCPAA system achieves a maximum gain of 21.8 dBi at the boresight with a high antenna efficiency of 88.4%. The scanning range reaches 51° for elevation and ±28° for azimuth with very small scanning loss and reasonably good cross polarization level. Overall, the compact and aerodynamic features of the proposed high-performance system make it promising for V2UA, V2X, DSR communications, radar sensing, etc.

ACKNOWLEDGMENT

The authors would like to thank Mr. Jiajun Li from École Polytechnique Fédérale de Lausanne for his valuable help and contribution in the cross-polarization measurement of the whole onboard system.

REFERENCES

[1] M. Nouri, H. Behroozi, A. Jafarieh, S. A. Aghdam, M. J. Piran, and N. K. Mallat, "A learning-based dipole Yagi-Uda antenna and phased array antenna for mmWave precoding and V2V communication in 5G systems," *IEEE Trans. Veh. Technol.*, vol. 72, no. 3, pp. 2789–2803, Mar. 2023.

[2] L. Qin, Y. Lu, Q. You, Y. Wang, J. Huang, and P. Gardner, "Millimeter-wave slotted waveguide array with unequal beamwidths and low sidelobe levels for vehicle radars and communications," *IEEE Trans. Veh. Technol.*, vol. 67, no. 11, pp. 10574–10582, Nov. 2018.

[3] H. Xu *et al*., "Single-fed dual-circularly polarized stacked dielectric resonator antenna for K/Ka-band UAV satellite communications," *IEEE Trans. Veh. Technol.*, vol. 71, no. 4, pp. 4449–4453, Apr. 2022.

[4] H. -L. Song and Y. -C. Ko, "Beam alignment for high-speed UAV via angle prediction and adaptive beam coverage," *IEEE Trans. Veh. Technol.*, vol. 70, no. 10, pp. 10185–10192, Oct. 2021.

[5] Y. -F. Cheng, Q. Chen, L. Peng, C. Liao, and X. Ding, "Dual-wideband structure-reused antenna with diverse radiation and polarization features for vehicular wireless communications," *IEEE Trans. Veh. Technol.*, (early access), doi: 10.1109/TVT.2023.3325449.

[6] Z. Chen, J. Tian, H. Liu, J. Yu, and X. Chen, "Novel pattern-diverse millimeter-wave antenna with broadband, high-gain, enhanced-coverage for energy-efficient unmanned aerial vehicle," *IEEE Trans. Veh. Technol.*, vol. 70, no. 5, pp. 4081–4087, May 2021.

[7] S. Y. Jun, A. Shastri, B. Sanz-Izquierdo, D. Bird, and A. McClelland, "Investigation of antennas integrated into disposable unmanned aerial vehicles," *IEEE Trans. Veh. Technol.*, vol. 68, no. 1, pp. 604–612, Jan. 2019.

[8] C. Wen, Y. Huang, J. Peng, G. Zheng, W. Liu, and J. -K. Zhang, "Reconfigurable sparse array synthesis with phase-only control via consensus-ADMM-based sparse optimization," *IEEE Trans. Veh. Technol.*, vol. 70, no. 7, pp. 6647–6661, Jul. 2021.

[9] W. Feng *et al*., "Joint 3D trajectory design and time allocation for UAV-enabled wireless power transfer networks," *IEEE Trans. Veh. Technol.*, vol. 69, no. 9, pp. 9265–9278, Sept. 2020.

[10] J. Wang *et al*., "Compact wideband circularly-polarized mechanically beam-steering antenna for Ka-band vehicular communications," *IEEE Trans. Veh. Technol.*, (early access), doi: 10.1109/TVT.2023.3327409.

[11] X. Fang, W. Wang, Y. Zheng, Z. Zheng, H. Zhang, and G. -L. Huang, "A compact and simply-constructed all-metal circularly polarized ridge-waveguide slotted antenna array for vehicle mounted satcom on the move (SOTM) communication application," *IEEE Trans. Veh. Technol.*, vol. 71, no. 12, pp. 12626–12634, Dec. 2022.

[12] C. J. Ma, B. J. Xiang, S. Y. Zheng, and Y. M. Pan, "A miniaturized planar multibeam antenna for millimeter-wave vehicular communication," *IEEE Trans. Veh. Technol.*, vol. 72, no. 3, pp. 3611–3621, Mar. 2023.

[13] L. Zhang *et al*., "A single-layer 10–30 GHz reflectarray antenna for the internet of vehicles," *IEEE Trans. Veh. Technol.*, vol. 71, no. 2, pp. 1480–1490, Feb. 2022.

[14] B. J. Xiang, X. Dai, and K. -M. Luk, "A wideband 2-bit transmitarray antenna for millimeter-wave vehicular communication," *IEEE Trans. Veh. Technol.*, vol. 71, no. 9, pp. 9202–9211, Sept. 2022.

[15] H. Bolandhemmat, M. Fakharzadeh, P. Mousavi, S. H. Jamali, G. Z. Rafi, and S. Safavi-Naeini, "Active stabilization of vehicle-mounted phased-array antennas," *IEEE Trans. Veh. Technol.*, vol. 58, no. 6, pp. 2638–2650, July 2009.

[16] M. Xu *et al*., "Low profile dynamic patch antenna array with high-intensity radiation fields (HIRF) protection," *IEEE Trans. Veh. Technol.*, vol. 71, no. 10, pp. 10527–10542, Oct. 2022.

[17] F. Karami, H. Boutayeb, L. Talbi, K. Hettak, and A. Ghayekhloo, "Multifunctional switched-beam antenna located on solar cell for vehicular to satellite communication," *IEEE Trans. Veh. Technol.*, (early access), doi: 10.1109/TVT.2023.3323419.

[18] C. Ren *et al*., "Study on the wide-angle scanning utilizing dual-port phased monopole antenna with corrugated structure," *IEEE Trans. Veh. Technol.*, vol. 72, no. 12, pp. 15463–15476, Dec. 2023.

[19] Z. N. Chen *et al*., "Microwave metalens antennas," *Proc. IEEE*, vol. 111, no. 8, pp. 978–1010, Aug. 2023.

[20] R.C. Hansen, "Conformal arrays", in *Significant Phased Array Papers*, MA: Artech House, 1973, pp. 211–228.

Accepted manuscript

[21] H. Zhu, X. Liang, S. Ye, R. Jin, and J. Geng, "A cylindrically conformal array with enhanced axial radiation," *IEEE Antennas Wireless Propag. Lett.*, vol. 15, pp. 1653–1656, 2016.
[22] S. Hussain, S. -W. Qu, P. Zhang, X. -H. Wang and S. Yang, "A low-profile, wide-scan, cylindrically conformal X-band phased array," *IEEE Antennas Wireless Propag. Lett.*, vol. 20, no. 8, pp. 1503–1507, Aug. 2021.
[23] Y. Liu, H. Yang, Z. Jin, F. Zhao, and J. Zhu, "A multibeam cylindrically conformal slot array antenna based on a modified Rotman lens," *IEEE Trans. Antennas Propag.*, vol. 66, no. 7, pp. 3441–3452, Jul. 2018.
[24] P. Wang, G. Wen, H. Zhang, and Y. Sun, "A wideband conformal end-fire antenna array mounted on a large conducting cylinder," *IEEE Trans. Antennas Propag.*, vol. 61, no. 9, pp. 4857–4861, Sept. 2013.
[25] V. Semkin *et al*., "Beam switching conformal antenna array for mm-wave communications," *IEEE Antennas Wireless Propag. Lett.*, vol. 15, pp. 28–31, 2016.
[26] M. Tang, Y. Duan, Z. Wu, and M. Li, "Flexible, conformal, endfire radiating, electrically small antennas on a conducting cylinder with a small radius," *IEEE Trans. Antennas Propag.*, vol. 68, no. 5, pp. 3496–3503, May 2020.
[27] C. Wu, L. C. Kempel, and E. J. Rothwell, "Mutual coupling between patch antennas recessed in an elliptic cylinder," *IEEE Trans. Antennas Propag.*, vol. 51, no. 9, pp. 2489–2492, Sept. 2003.
[28] V. B. Erturk, O. Bakir, R. G. Rojas, and B. Guner, "Scan blindness phenomenon in conformal finite phased arrays of printed dipoles," *IEEE Trans. Antennas Propag.*, vol. 54, no. 6, pp. 1699–1708, Jun. 2006.
[29] Z. Zhang, X. Gao, W. Chen, Z. Feng, and M. F. Iskander, "Study of conformal switchable antenna system on cylindrical surface for isotropic coverage," *IEEE Trans. Antennas Propag.*, vol. 59, no. 3, pp. 776–783, Mar. 2011.
[30] S. Raffaelli, Z. Sipus and P. -. Kildal, "Analysis and measurements of conformal patch array antennas on multilayer circular cylinder," *IEEE Trans. Antennas Propag.*, vol. 53, no. 3, pp. 1105–1113, Mar. 2005.
[31] V. B. Erturk and R. G. Rojas, "Efficient analysis of input impedance and mutual coupling of microstrip antennas mounted on large coated cylinders," *IEEE Trans. Antennas Propag.*, vol. 51, no. 4, pp. 739–749, Apr. 2003.
[32] H. Yang, X. Liu, and Y. Fan, "Design of broadband circularly polarized all-textile antenna and its conformal array for wearable devices," *IEEE Trans. Antennas Propag.*, vol. 70, no. 1, pp. 209–220, Jan. 2022.
[33] W. Hu, X. Wang, Y. Li, and S. Xiao, "Synthesis of conformal arrays with matched dual-polarized patterns," *IEEE Antennas Wireless Propag. Lett.*, vol. 15, pp. 1341–1344, 2016.
[34] S. Yu, N. Kou, J. Jiang, Z. Ding, and Z. Zhang, "Beam steering of orbital angular momentum vortex waves with spherical conformal array," *IEEE Antennas Wireless Propag. Lett.*, vol. 20, no. 7, pp. 1244–1248, Jul. 2021.
[35] B. D. Braaten, S. Roy, I. Irfanullah, S. Nariyal, and D. E. Anagnostou, "Phase-compensated conformal antennas for changing spherical surfaces," *IEEE Trans. Antennas Propag.*, vol. 62, no. 4, pp. 1880–1887, Apr. 2014.
[36] C. Dohmen, J. W. Odendaal and J. Joubert, "Synthesis of conformal arrays with optimized polarization," *IEEE Trans. Antennas Propag.*, vol. 55, no. 10, pp. 2922–2925, Oct. 2007.
[37] Z. Sipus, S. Skokic, M. Bosiljevac, and N. Burum, "Study of mutual coupling between circular stacked-patch antennas on a sphere," *IEEE Trans. Antennas Propag.*, vol. 56, no. 7, pp. 1834–1844, Jul. 2008.
[38] T. V. B. Giang and A. Dreher, "Analysis method of microstrip antennas on hemispherical multilayer structures," *IEEE Trans. Antennas Propag.*, vol. 56, no. 10, pp. 3324–3327, Oct. 2008.
[39] W. T. Li, C. Cui, X. T. Ye, X. W. Shi and H. C. So, "Quasi-time-invariant 3-D focusing beampattern synthesis for conformal frequency diverse array," *IEEE Trans. Antennas Propag.*, vol. 68, no. 4, pp. 2684–2697, Apr. 2020.
[40] H. M. Bernety, S. Venkatesh and D. Schurig, "Analytical phasing of arbitrarily oriented arrays using a fast, analytical far-field calculation method," *IEEE Trans. Antennas Propag.*, vol. 66, no. 6, pp. 2911–2922, Jun. 2018.
[41] J.-J. Peng, S.-W. Qu, M. Xia, and S. Yang, "Wide-scanning conformal phased array antenna for UAV radar based on polyimide film," *IEEE Antennas Wireless Propag. Lett.*, vol. 19, no. 9, pp. 1581–1585, Sep. 2020.
[42] Y. Qiang, L. Guo, M. Jing, and Q. Lai, "A design of conformal dipole array for aircraft applications," in *IEEE Int. Conf. Microw. Millimeter Wave Technol. (ICMMT 2016)*, Beijing, China, 2016, pp. 464–466.
[43] M. Kanno, T. Hashimura, T. Katada, M. Sato, K. Fukutani, and A. Suzuki, "Digital beam forming for conformal active array antenna," in *Proc. Int. Symp. Phased Array Syst. Technol.*, Boston, MA, USA, 1996, pp. 37–40.
[44] J. L. Kmetzo, "An analytical approach to the coverage of a hemisphere by N planar phased arrays", *IEEE Trans. Antennas Propag.*, vol. AP-15, no. 3, pp. 367-371, May 1967.
[45] H. S. Lin, Y. J. Cheng, Y. F. Wu and Y. Fan, "Height reduced concave sector-cut spherical conformal phased array antenna based on distributed aperture synthesis," *IEEE Trans. Antennas Propag.*, vol. 69, no. 10, pp. 6509–6517, Oct. 2021.
[46] D. Nikolayev, A. Mazzinghi and A. K. Skrivervik, "Rapid analysis of arbitrary-shaped conformal beam-scanning arrays," in *2020 14th Eur. Conf. Antennas Propag. (EuCAP)*, 2020, pp. 1–4, doi: 10.23919/EuCAP48036.2020.9135832.
[47] I. V. Soares, P. Vadher, A. K. Skrivervik, G. Sacco, and D. Nikolayev, "Analysis of non-canonical body-conformal arrays with polarization decomposition", in *Proc. 2023 17th Eur. Conf. Antennas Propag. (EuCAP)*, 2023, pp. 1–5.
[48] Z. Shao and Y. Zhang, "A single-layer miniaturized patch antenna based on coupled microstrips," *IEEE Antennas Wireless Propag. Lett.*, vol. 20, no. 5, pp. 823–827, May 2021.
[49] Analog Devices, 2023, *GaAs MMIC 6-BIT Digital Phase Shifter HMC1133LP5E Data Sheet.* [Online]. Available: https://www.analog.com/media/en/technical-documentation/data-sheets/hmc1133.pdf
[50] Mini-Circuits, 2017, *4 Ways MMIC Power Splitter WP4A+ Data Sheet*. [Online]. Available: https://www.minicircuits.com/pdfs/WP4A+.pdf
[51] Mini-Circuits, 2017, *2 Ways LTCC Power Splitter SCN-2-65/65+ Data Sheet*. [Online]. Available: https://www.minicircuits.com/pdfs/SCN-2-65+.pdf

Yuanyan Su received her M.S. and Ph.D. degrees in electrical and computer engineering from National University of Singapore, Singapore, in 2014 and 2019, respectively.

In 2015 and 2019, she was a research assistant and visiting scholar with the research teams of State Key Laboratory of Millimeter Waves, Southeast University, Nanjing, China. From 2020 to 2024, she was a Post-Doctoral Fellow at Microwaves and Antennas Group, École Polytechnique Fédérale de Lausanne, Lausanne, Switzerland. She is currently an Associate Professor at Nanjing University of Aeronautics and Astronautics, Nanjing, China, since 2024. Her research interests include advanced microwave resonators for atomic frequency standards, Luneburg lens antennas, miniature beamscanning antennas and phased arrays, beamforming techniques, and material characterization methods.

Icaro V. Soares (Member, IEEE) received his M.Sc. and Ph.D. degrees in Electronic Engineering from the Federal Center for Technological Education of Minas Gerais (CEFET-MG), Brazil, and the Université de Rennes, France, in 2020 and 2023, respectively.

He was an Electrical Engineer at Stellantis South America until 2019 and then an R&D Electronic Engineer at IBBx Innovation until 2020. He is currently a postdoctoral fellow at Institut d'Electronique et des Technologies du numéRique (IETR) in Rennes, France. His expertise is in Applied Electromagnetism, and his research interests include wireless power transfer and energy harvesting techniques, implantable and wearable bioelectronics, and numerical analysis of electromagnetic systems. He received the Student Presentation Award at BioEM 2021 and the Best Thesis award from the Foundation Université de Rennes in 2024.

Accepted manuscript

Siegfred Balon (M'14) received B.S. and M.S. degrees from University of the Philippines – Diliman in 2009 and 2011, respectively, and Ph.D. degree from National University of Singapore in 2019.

He is currently a Principal Engineer at Desay SV Automotive in Singapore where he is heavily involved in automotive radar signal processing development, MIMO array and systems design, UWB radar and wireless sensing. Prior to his current affiliation, he was a post-doctoral research fellow at National University of Singapore, working on synthetic aperture radar imaging systems. His research interests include microwave and RF systems, synthetic aperture radar imaging, digital beamforming and MIMO radars, algorithm design for automotive radars and sensor fusion technologies, UWB-based bioradar and WiFi living object presence detection, and the integration of machine learning in these signal processing applications.

Jun Cao received his M.Eng. in signal processing and Ph.D. degrees in neuroscience from Beijing Institute of Technology and The University of New South Wales, in 2016 and 2022, respectively.

From 2017 to 2018, he worked as a research engineer in human fall detection based on microwave imaging at National University of Singapore. Since 2022, he is a Post-Doctoral Fellow with Neuroscience Research Australia. His research interest includes advanced brain imaging techniques, new biomarkers for brain activity and diseases, and brain imaging analysis.

Denys Nikolayev (Senior Member, IEEE) received his M.Sc. degree *summa cum laude* in applied electromagnetics from Lviv Polytechnic National University, Ukraine, in 2008. He earned dual Ph.D. degrees in electronics from the IETR laboratory of the French National Center for Scientific Research (CNRS), France, and in electrical engineering from the University of West Bohemia in Pilsen, Czechia, in 2017. In 2023, he obtained the "*Habilitation à Diriger des Recherches*" (HDR) degree from the University of Rennes, France.

He served as a Postdoctoral Fellow at imec/Ghent University, Belgium, until 2018, followed by a position of a Scientist at the École Polytechnique Fédérale de Lausanne (EPFL), Switzerland, until 2020. He then joined the French National Center for Scientific Research (CNRS) as a Senior Scientist. His research focuses on the theoretical foundations and engineering of wireless bioelectronics. His work has been recognized with several awards, including the Best Ph.D. Dissertation Award from the Fondation Rennes 1. He is a laureate of the Eiffel Excellence Doctoral Fellowship and the recipient of the ANR–NRF PRCI Research Fellowship (2021), jointly awarded by the Agence Nationale de la Recherche, France, and the National Research Foundation, Singapore. Since 2022, he has served as an elected member of the Section 8 of the French National Committee for Scientific Research.

Anja K. Skrivervik received her Master degree and Ph.D. in electrical engineering from Ecole Polytechnique Fédérale de Lausanne (EPFL) in 1986 and 1992, respectively, for latter she received the Latsis award.

After a stay at the University of Rennes as an invited Research Fellow and two years in the industry, she returned part time to EPFL as an Assistant Professor in 1996, and is now a Professeur Titulaire at this institution, where she is the head of the Microwave and Antenna Group. She is also a visiting Professor at the University of Lund. Her research activities include electrically small antennas, antennas in biological media, periodic structures, reflect- and transmitarrays, and numerical techniques for electromagnetics. She is author or co-author of more than 200 peer reviewed scientific publications.

She is very active in European collaboration and European projects. She was the chairperson of the Swiss URSI until 2012, is a Board member of the European School on Antennas and is frequently requested to review research programs and centers in Europe. She was a member of the board of directors of the European Association on Antennas and Propagation (EurAAP) from 2017 to 2022. She has been the general Chair of the Loughborough Antenna and Propagation Conference in 2015, Vice-Chair and Technical Program Committee-Chair of EuCAP 2016 conference and financial chair of EuCAP 2017 to EuCAP 2022.

Accepted manuscript